Layer‐by‐Layer‐Processed Organic Solar Cells with 18.02% Efficiency Enabled by Regulating the Aggregation of Bottom Polymers

Xing Wu,[†] Yixuan Wu,[†] Shichu Peng,[†] Liangang Xiao,*[,†] Zijie Xiao,[§] Wei Zhang,*[,§] Guoxing Ren,[†] Yonggang Min*[,†] and Yi Liu*[,‡]

[†]School of Materials and Energy, Guangdong University of Technology, Guangzhou 510006, China

E-mail: xiaolg@gdut.edu.cn, ygmin@gdut.edu.cn

[‡]The Molecular Foundry, Lawrence Berkeley National Laboratory, Berkeley, CA, 94720, USA

E-mail: yliu@lbl.gov

[§]School of Physics and Materials Science, Guangzhou University, Guangzhou, 510006, China

E-mail: wzhang@gzhu.edu.cn

Keywords: carrier recombination, layer-by-layer, organic solar cells, pre-aggregation, vertical phase separation

Abstract

The fabrication of organic solar cells (OSCs) by a layer-by-layer (LBL) method has attracted growing attention in recent years. Finely tuning the molecular packing and crystallinity to obtain films with suitable morphology is crucial for fabricating OSCs with high photovoltaic performance. The pre-aggregates of conjugated polymers in solution have a profound impact on their packing and morphology in thin films. Thanks to temperature-controlled pre-aggregation in solution, the crystallinity and microstructures of polymer thin films could be finely tuned. Such control enables

bilayer OSC devices based on the polymer donor D18 and the non-fullerene acceptor L8-BO to deliver an enhanced power conversion efficiency (PCE) of 17.10% compared to the 16.43% PCE of the bulk heterojunction devices. In addition, after further treating the D18 films through a combined thermal and solvent vapor annealing (TA&SVA) process, the corresponding LBL OSCs devices have delivered a champion PCE of 18.02% with simultaneously improved current density (J_{SC}) of 26.43 mA cm^{-2}, open-circuit voltage (V_{OC}) of 0.927 V and fill factor (FF) of 73.52%. These results demonstrate that the LBL deposition process utilizing the pre-aggregation of polymer and its fiber network forming ability is a very promising approach to improving charge dynamics, suppressing carrier recombination and fabricating highly efficient OSCs.

1. Introduction

Solution-processed organic solar cells (OSCs), as one of the most potential candidates for renewable energy in the near future, have attracted increasing attention due to their unique advantages of lightweight, mechanical flexibility and high throughput production when combined with industrial roll-to-roll manufacturing.[1-7] In recent years, the rapid development of novel photovoltaic materials and ingenious device structures, combined with the deep understanding of device physics, have pushed the photovoltaic performance of the bulk heterojunction (BHJ) to reach a milestone with the highest power conversion efficiency (PCE) more than 19%, leading to bright application prospects of OSCs in meeting the rapidly growing demand for green energy.[8-10] Device structure evolution had experienced the transition from the original single-component single layer structure to a double-layer structure containing one electron donor (D) and one electron acceptor (A), which could enhance exciton separation at the D/A interface. However, the intrinsic property of short diffusion length of the excitons determines that most excitons cannot reach the interface and separate into electron and hole. In 1995, Yu et al. firstly reported the BHJ structure OSCs based on the blend film containing D:A mixture in a single layer. Compared to the previously studied device structure, BHJ structure greatly promoted the exciton diffusion and charge separation efficiency, and has since become the most important device structure,

leading the rapid development of organic photovoltaic technology in the following years.[11-13]

In spite of the great progress of BHJ OSCs, there are various inevitable shortcomings, such as isolated donor and acceptor islands and unsuitable vertical phase distribution in the blend films, which are unfavorable for charge transport and increase the probability of charge recombination. Furthermore, when spin-coating the solution of donor and acceptor mixtures, the crystallization and packing properties of the donor and acceptor would interfere mutually, resulting in complex kinetic problems for regulation of the morphology of the active layer during the film evolution process.[14-18] When donors and acceptors in the solution are mixed inadequately or too well, the BHJ OSCs always deliver a poor PCE and inferior device stability. Especially for OSCs based on widely used non-fullerene acceptors, the similar chemical structures of electron donors and acceptors doomed them to be over mixed. Therefore, arduous efforts are needed to realize phase separation at a suitable length scale and a good vertical component distribution.[19] The layer-by-layer (LBL) structure fabricated by sequentially depositing D and A in separate solutions could not only provide the opportunities to hierarchically manipulate the microstructure morphology of D/A double layers, but also is conducive to the formation of vertical component distribution. In addition, owing to molecular diffusion and penetration and solvent-induced swelling, D/A interface with suitable nanoscale separation could also be successfully formed for efficient exciton separation. Consequently, high-purity domains mainly exist in the bottom D layer and the top A layer, and the separated holes and electrons could transport efficiently in the D phase and A phase to the corresponding electrodes, respectively. These characteristics of LBL structured devices make them very promising for achieving high-performance OSCs[20-21] and also for large-area OSCs.[22-23] In very recent years, OSCs based on LBL method have attracted enormous attention.[24-30] A lot of efforts have been devoted to elevating the photovoltaic performance to an acceptable PCE, mainly involving the addition of a third photovoltaic material for fabricating ternary LBL OSCs,[31-32] optimizing the morphology using suitable additives,[33-36] and synthesizing novel materials for manipulating their electronic and solubility

properties.[37-38] However, the study of morphology control in LBL OSCs is significantly lagged behind compared with the BHJ ones. Therefore, alternative approaches for regulating molecular aggregation in solution and packing in thin films in LBL devices are critically needed.

Aggregation in solution state is a very common phenomenon for conjugated polymers. The pre-aggregates of conjugated polymers in solution have a profound impact on their packing and morphology in thin films, and therefore their charge transport and photovoltaic performance.[39-42] Recently, enormous efforts have been devoted to controlling polymer film microstructures by using the synergistic effect of solvent and temperature on polymer aggregation in solution.[43-46] However, there still remains significant challenges for controlling microstructures and regulating structural evolution across different length scales. Generally, the conformation of conjugated polymer backbones in solution is strongly dependent on temperature. Deliberate temperature control could offer a simple means to regulate polymer aggregates in solution, and subsequently to realize ordered packing structures and suitable morphology in thin films.

In this contribution, the wide bandgap polymer donor D18[47] (Scheme 1) and the narrow bandgap small molecule non-fullerene acceptor L8-BO[48] (Scheme 1) were employed to fabricate highly efficient LBL OSCs. By simply controlling the solution temperature, we could effectively fine-tune pre-aggregation state of polymer donor D18 in solution and therefore its solid-state film morphology in the bottom layer of LBL OSCs. The underlying microstructures of D18 have a significant effect on the formation of the upper L8-BO films and the charge transport and photovoltaic performance of devices. Combined thermal and solvent vapor annealing treatment further enhanced the film's morphology, which effectively suppressed charge recombination and improved photovoltaic performance of D18/L8-BO based LBL OSCs devices from 17.10% to 18.02% with significantly enhanced current density (J_{SC}), open-circuit voltage (V_{OC}) and fill factor (FF). The time-of-flight secondary ion mass spectrometry (TOF-SIMS) measurement revealed that the L8-BO layer evenly penetrated into the D18 layer such that a vertical phase separation with a special D/D:A/A structure (P-i-N type component

distribution) was formed. Such structure was responsible for an obviously higher device PCE when compared to the BHJ counterpart (16.37%). This study provided a simple approach for fabricating highly efficient LBL OSCs via control of solution aggregation behavior, and also demonstrated the great potential of LBL fabrication method in regulating microstructure of active layers and suppressing carrier recombination in devices.

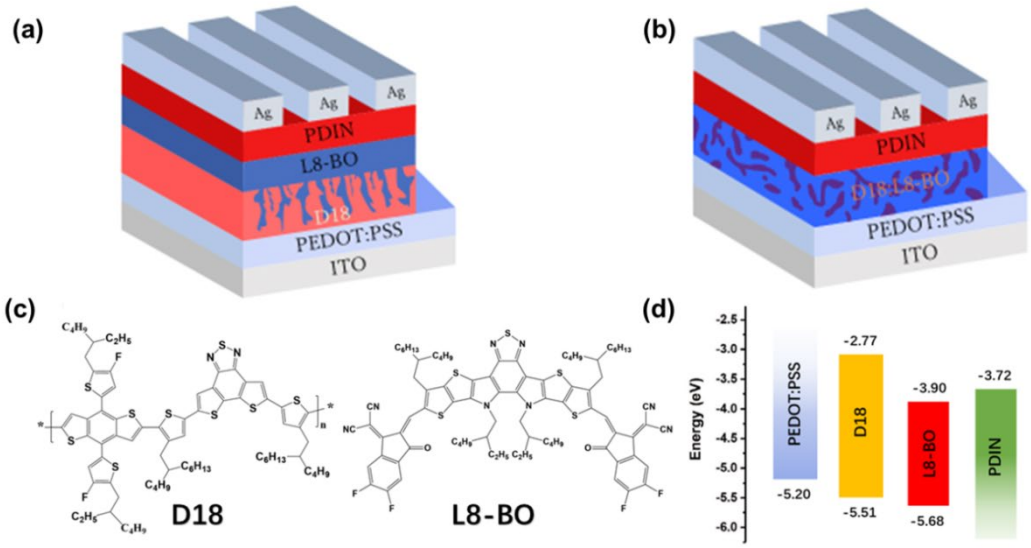

Scheme 1. (a) The device structure of LBL type solar cells. (b) The device structure of BHJ type solar cells. (c) Chemical structures of D18 and L8-BO. (d) Energy levels of PEDOT:PSS, D18, L8-BO, and PDIN.

2. Results and Discussions

The evaporation time of chlorobenzene solvent and aggregate formation of D18 polymer in solvent were varied at different temperatures. When the dissolved D18 was placed at room temperature for about ten minutes, the D18 solution became a gel and lost most of its fluidity (Figure S1). The viscosity of the D18 solution decreased and the D18 solution exhibited good solution processability when the temperature was higher than 30 ℃. As shown in Figure 1a and Figure 1b, the D18 in solution and in a thin film under different processing conditions show dual-band absorption

spectra. The absorption peak of D18 in dilute solution mainly locates at 585 nm, and there is no obvious peak shifts from solution to film, which indicates that the aggregates of D18 may be predestined even in dilute solution because of the strong intermolecular interactions of D18. In addition, the crystallization process of polymers consists of nucleation and growth, and therefore aggregate structures in solution would affect the packing in films.[49] We postulate that there are some differences between solid-state packing structures of D18 thin films processed from solutions at different temperatures. When comparing the extinction coefficients of D18 films obtained from different processing conditions, the film processed from solution at 30 ℃ showed the lowest absorption coefficient of 6.0×10^4 cm^{-1}, and films processed from solution at 60 ℃ and processed from solution at 60 ℃ further with TA&SVA showed obviously larger extinction coefficients of 6.6×10^4 cm^{-1} and 6.8×10^4 cm^{-1}, respectively. The gradually enhanced extinction coefficient indicated the improved film crystallinity. More importantly, it could also be observed that there were some distinctions in the relative intensity of the absorption peaks under different processing conditions. The ratio of absorption peaks $I_{0\text{-}0}/I_{0\text{-}1}$ of D18 films increased from 1.04 to 1.10 when the processing temperature was elevated from 30 ℃ to 60 ℃, and a slight decrease to 1.09 when the temperature was further raised to 90 ℃. When the film was sequentially treated with TA&SVA, the ratio was further enhanced from 1.10 to 1.12, which justified a more planar backbone structure (π-π stacking) of D18. The improved crystallinity and planar stacking were believed to contribute to hole transport in D8 thin films. The extinction coefficients of D18/L8-BO bilayer films based on D18 processed under different conditions were illustrated in Figure S2. When the temperature of D18 solution was elevated from 30℃ to 60 ℃, a 7 nm redshift of the characteristic L8-BO molecule peak was observed (the Figure S3), which suggested the more ordered packing of L8-BO.[50]

LBL OSC devices with a structure of ITO/PEDOT:PSS/D18/L8-BO/PDIN/Ag (Scheme 1a) were fabricated under different film processing conditions to investigate the corresponding photovoltaic performance. In addition, BHJ solar cells with a device

structure of ITO/PEDOT:PSS/D18:L8-BO/PDIN/Ag (Scheme 1b) were also fabricated. The chemical structures and energy levels of D18 and L8-BO were shown in Scheme 1b and Scheme 1c, respectively. The optimized *J*−*V* curves based on D18/L8-BO LBL OSCs devices were shown in Figure 1c, and the corresponding photovoltaic parameters were summarized in Table 1. LBL devices with D18 bottom layer processed from solution at 30 ℃ exhibited a moderate PCE of 16.43% with a low J_{SC} of 24.54 mA cm $^{-2}$, a V_{OC} of 0.918 V, and a FF of 72.91%. When the processing temperature of the D18 bottom layer was elevated to 60 ℃, the corresponding LBL OSC device exhibited an enhanced efficiency of 17.10% accompanied with a J_{SC} of 25.98 mA cm^{-2}, a V_{OC} of 0.919 V, and a FF of 71.64%. A slightly decreased efficiency was observed for the device based on the D18 bottom layer processed from solution at 90 ℃. When an additional TA&SVA process was applied to the bilayer device based on a D18 bottom layer casted from solution at 60 ℃, the devices exhibited a significantly enhanced PCE of 18.02% with simultaneously improved J_{SC} of 26.43 mA cm^{-2}, V_{OC} of 0.927 V, and FF of 73.52%. In addition, the optimized photovoltaic parameters of BHJ OSCs and LBL OSCs based on D18 processed from chloroform were also listed Table S1-S3. The optimized BHJ devices and LBL devices based on D18 processed from chloroform delivered a lower PCE of 16.37% and 14.78%, respectively. To verify the accuracy of the *J*-*V* measurements, the external quantum efficiency (EQE) spectra of all devices were characterized and shown in Figure 1d. The J_{SC} values obtained from EQE spectra integration were consistent with the values obtained from *J*-*V* measurements under standard solar simulator. All the devices presented a broad photo-response range from 300 to 900 nm. Notably, the EQE values of the optimized devices (60 ℃+TA&SVA) were higher than that of other devices, in accordance with the contrasting absorption spectra of the D18 and D18/L8-BO films processed under different conditions.

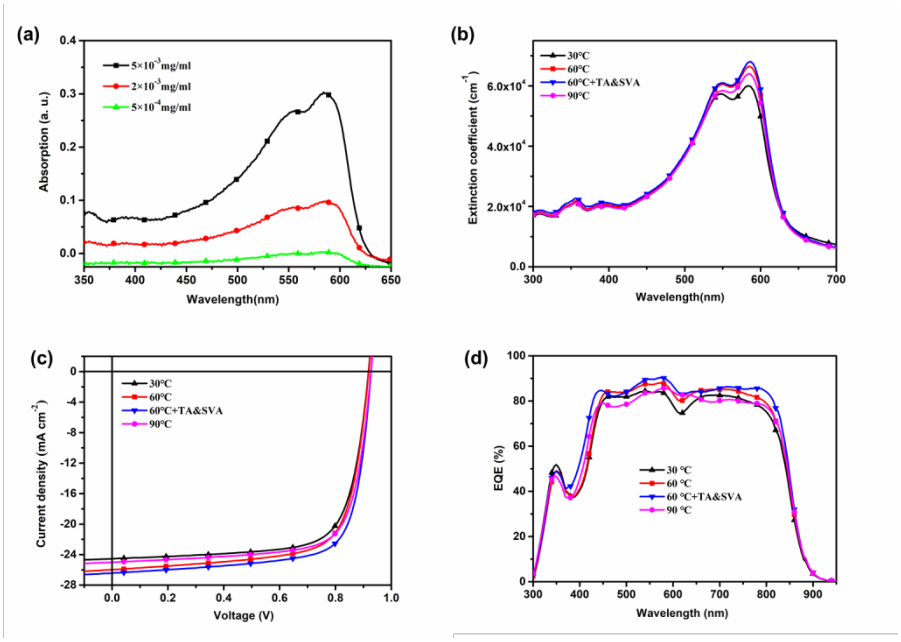

Figure 1. The extinction coefficients of D18 in solution (a) and in thin films (b) under different processing conditions; the optimized *J*−*V* curves (c) and EQE curves (d) based on D18 and L8-BO LBL OSCs devices.

Table 1 Photovoltaic parameters for D18/L8-BO-based solar cells under different processing conditions.

Condition	J_{SC} (mA cm^{-2})	V_{OC} (V)	FF%	PCE%
Control (30 °C)	24.54	0.918	72.91	16.43[a] (16.28)[b]
60 °C	25.98	0.919	71.64	17.10[a] (16.97)[b]
60 °C+TA&SVA	26.43	0.927	73.52	18.02[a] (17.90)[b]
90°C	25.00	0.927	73.49	17.03[a] (16.88)[b]

a) the best PCE; b) values in parentheses are average PCEs from ten devices.

The dependence of the photo-generated current density (J_{ph}) on the effective voltage (V_{eff}) was measured to investigate the charge dynamics (exciton dissociation and charge collection processes) of LBL processed OSCs devices (Figure 2a). Herein, J_{ph} and V_{eff} are defined as J_{ph}=J_L-J_D and V_{eff}=V_0-V, respectively (J_L and J_D are current densities under illumination and in the dark, V_0 is the voltage where J_{ph} is 0, and V is the applied voltage).[51-52] J_{ph} would become saturated (J_{sat}) when devices are under a

high reverse bias voltage regime, and almost all excitons are dissociated into free carriers and further collected to the electrodes. The related physical parameters of devices under various processing conditions (Table S4) are also employed to evaluate charge dissociation probabilities (*P(E,T)*).[53] *P(E,T)* was calculated as the J_{ph}/J_{sat} ratio under short-circuit current condition. The *P(E,T)* values were 92.3%, 94.0%, 94.1% and 94.1% for the devices based on the D18 processed from the conditions of 30 ℃, 60 ℃, 60℃+TA&SVA and 90 ℃, respectively. Moreover, according to the equation of $J_{sat}=qG_{max}L$, the corresponding maximum exciton generation rate (G_{max}) values were calculated to be 1.41×10^{28}, 1.44×10^{28}, 1.47×10^{28} and 1.40×10^{28} m^{-3} s^{-1}, respectively. The increased G_{max} for the device based on the D18 processed from the conditions of 60 ℃ and 60 ℃+TA&SVA is consistent with the enhanced *J*sc, which is probably derived from enhanced absorption and more ordered packing. These results show that devices based on D18 processed from the condition of 60℃+TA&SVA exhibits enhanced charge dynamics with best exciton dissociation efficiency.

To further understand the recombination processes in different devices, we measured the *J-V* characteristics under different light intensities (P_{light}) and plotted the dependence of J_{SC} and V_{OC} on P_{light}. The relationship between J_{SC} and P_{light} can be described as $J_{SC} \propto (P_{light})^S$, where the power-law exponential factor S characterizes the degree of bimolecular recombination. Generally, an S value very close to 1 indicates that the bimolecular recombination in devices can be ignored. As shown in Figure 2b, the fitted S values are 0.90, 0.91, 0.95, and 0.91 for devices based on D18 fabricated under the processing conditions of 30 ℃, 60 ℃, 60 ℃+TA&SVA and 90 ℃, respectively. These results indicate the most reduced bimolecular recombination from the LBL devices based on D18 processed under the condition of 60℃+TA&SVA, manifesting that the processing temperature of D18 has no obvious effect on bimolecular recombination, but the subsequent TA&SVA process has a notable effect on suppressing bimolecular recombination. Furthermore, as shown by the plots of V_{OC} versus P_{light} in Figure 2c, the device based on D18 processed from solution at 30 ℃ features the largest slope of 1.80 k_BT/q. This indicated severe trap-assisted Shockley-Read-Hall (SRH) or geminate recombination.[54-56] The slopes decreased to 1.54 k_BT/q

and 1.34 k_BT/q for the devices based on D18 fabricated under the processing conditions of 60 ℃ and 60 ℃+TA&SVA, respectively. The smallest slope of 1.34 k_BT/q suggested that the SRH or geminate recombination were effectively suppressed. Taken together, the suppressed charge recombination should be favorable for more efficient exciton dissociation and charge transport.

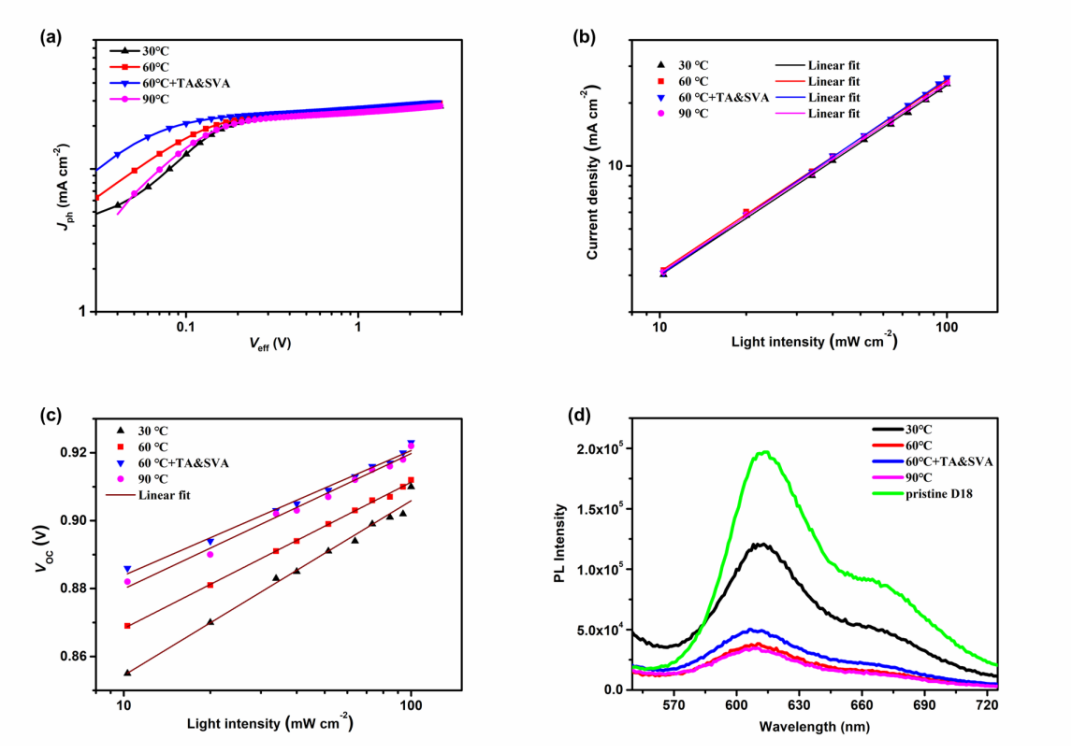

Figure 2. (a) the J_{ph}-V_{eff} curves of representative LBL solar cells, (b) the dependence of J_{SC} on light intensity of representative LBL solar cells, (c) the dependence of V_{OC} on light intensity of representative LBL solar cells, (d) PL spectra of D18 and D18/L8-BO bilayer films based on D18 fabricated under different processing conditions.

The charge transport properties of the D18/L8-BO bilayer films based on D18 processed under different processing conditions were evaluated by applying the space charge limited current (SCLC) method (Figure 3), and the corresponding data were summarized in Table S5. The structures of hole-only and electron-only devices are ITO/PEDOT:PSS/D18/L8-BO/Ag and ITO/ZnO/D18/L8-BO/PDIN/Ag, respectively. Devices based on D18 processed from solution at 30 ℃ exhibited a hole mobility (μ_h) of 3.06×10^{-4} cm^2 V^{-1} s^{-1} and an electron mobility (μ_e) of 3.93×10^{-4} cm^2 V^{-1} s^{-1}. When

the processing temperature of D18 was elevated to 60 ℃, the devices showed the enhanced charge transport properties with hole and electron mobilities measured to be 5.66×10^{-4} cm^2 V^{-1} s^{-1} and 4.00×10^{-4} cm^2 V^{-1} s^{-1}, respectively. However, the μ_h and μ_e were decreased when the processing temperature was further increased to 90 ℃. In addition, for the D18 films processed from solution at 60 ℃ and further treated with TA&SVA, the hole and electron mobilities were simultaneously elevated to 8.35×10^{-4} cm^2 V^{-1} s^{-1} and 7.00×10^{-4} cm^2 V^{-1} s^{-1}, respectively. The more balanced charge transportation, as indicated by a μ_h/μ_e ratio closer to 1, suggested the effectively suppressed charge accumulation, contributing to the reduced charge recombination and enhanced J_{SC} in the optimized device.

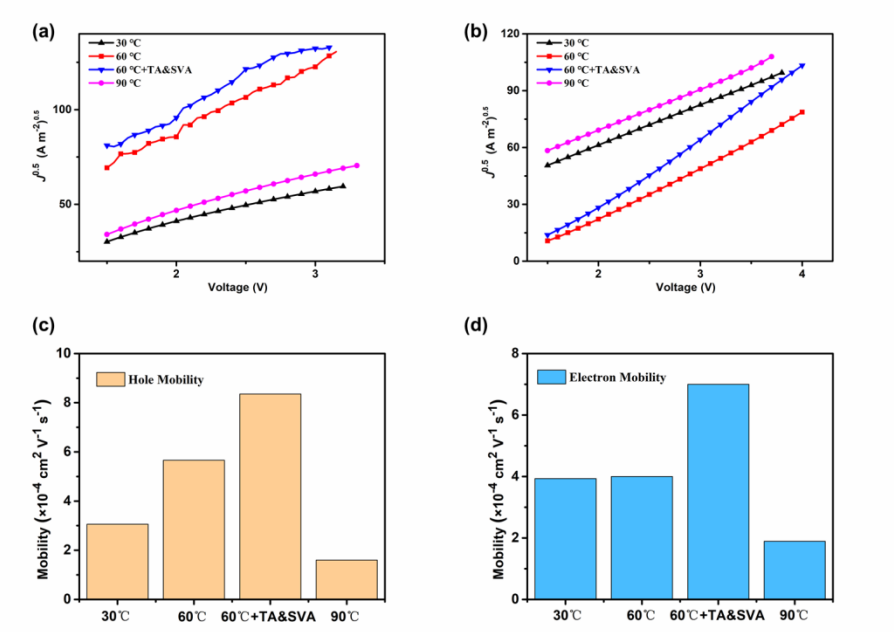

Figure 3. *J-V* curve of (a) hole-only and (b) electron-only devices based on D18 fabricated under different processing conditions, (c) hole mobility and (d) electron mobility of devices based on D18 fabricated under different processing conditions.

Efficient exciton dissociation and charge transfer at the D/A interface are crucial for delivering high PCE devices.[57-59] To further investigate the exciton dynamic processes, steady-state photoluminescence (PL) spectra of pristine D18 film and D18/L8-BO bilayer films were performed and corresponding spectra were illustrated

in Figure 2d. The excitation energy of 467 nm was employed to excite D18 in these films. D18 showed a characteristic emission peak at 610 nm, and the PL intensity of D18/L8-BO bilayer films at this peak showed obvious quenching. Compared to the bilayer film based on D18 processed from solution at 30 ℃, the PL of films processed at higher temperature was more effectively quenched, suggesting better exciton dissociation and charge transfer at the interfaces of D18/L8-BO bilayer films. After the D18 films (processed from solution at 60 ℃) were further treated with TA&SVA, the quenching extent was slightly alleviated. This trend was probably due to the enlarged crystalline domains size during the annealing processes that resulted in higher radiative recombination of exciton before reaching the interface and suppressing nonradiative recombination through trap-states, which correlated well with the results mentioned above. It can be concluded that appropriate phase separation of bilayer films is responsible for the higher electron and hole mobilities, suppressed recombination and consequently higher PCE.

To gain more insight into the working mechanism behind the higher PCE, transient absorption (TA) spectroscopy was employed to study the charge photogeneration processes in the D18/L8-BO bilayer films under various processing conditions. By selectively exciting the L8-BO in bilayer films at 800 nm, we observed an ultrafast formation of ground state bleaching (GSB) peaks of L8-BO at ~820 nm and D18 at ~590 nm, as shown in Figure 4a. Since 800 nm laser cannot excite the donor materials (D18) in the blend, the ultrafast formation of GSB peaks of D18 indicates that there is a fast hole transfer process from the L8-BO to D18. Besides, we observed that the ~820 nm peak decayed while the ~590 nm peak rose, manifesting a slower hole transfer process at the D/A interface. In the GSB kinetics of the blend films under 30 ℃ and 60 ℃+TA&SVA conditions (Figure 4b and Figure S4-S5), the fast and slow rise processes are more obviously. Here, the fast and slow hole transfer processes can be attributed to direct exciton dissociation of acceptors around the interface and diffusion mediated exciton dissociation, respectively. We found that the direct exciton dissociation time (τ_1~0.75 ps) was similar for the two bilayer films, while the time for diffusion mediated exciton dissociation in the bilayer film based on D18 processed

under the condition of 60 ℃+TA&SVA (τ_2~10.7 ps) was slightly longer than that based on D18 processed at the condition of 30 ℃ (τ_2~9.4 ps). Diffusion mediated exciton dissociation is strongly controlled by D-A domain size and aggregation. The increases of τ_2 value suggested that the average size of the L8-BO acceptor phase for the 60℃+TA&SVA processed bilayer film was slightly larger than that of the film processed under 30 ℃.[60-61] Furthermore, we examined the carrier recombination processes in the ultrafast timescale by fitting the decay kinetics of the 590 nm peak with double exponential decay functions (Table S6). Charge recombination rate for the bilayer film based on D18 processed at 30 ℃ was generally faster than that processed at 60 ℃+TA&SVA, suggesting that the bilayer film based on D18 processed under the condition of 60 ℃+TA&SVA has the advantage of suppressing charge recombination in the ultrafast timescale.

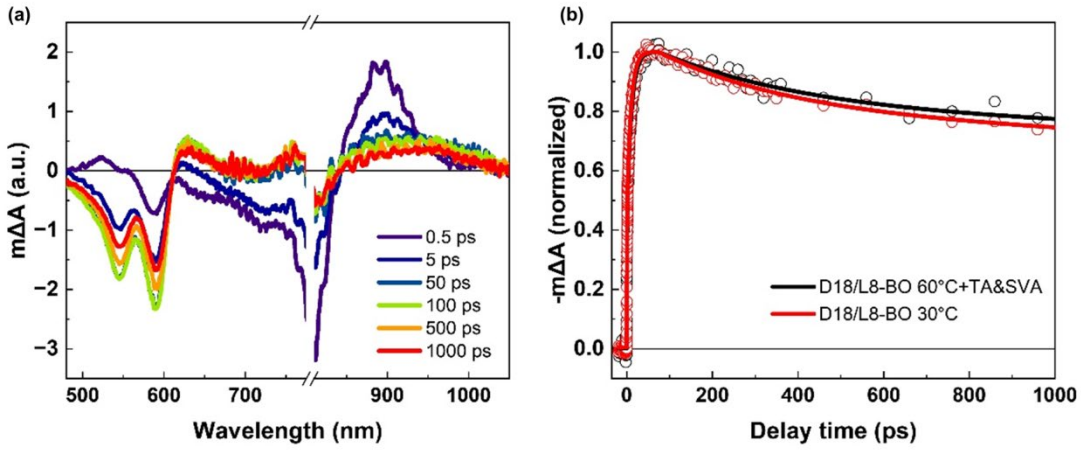

Figure 4 (a) TA spectra of D18/L8-BO blend film obtained from 60 ℃+TA&SVA at indicated delay time; (b) TA kinetics of D18/L8-BO blend films obtained from 30 ℃ and 60 ℃+TA&SVA with a probe wavelength of ~590 nm. The solid lines are fitting curves based on multiple-exponential functions, and the fitting parameters can be found in supporting information. The excitation wavelength is ~800 nm and the excitation fluence is 3.6×10^{13} $cm^{-2} \cdot pulse^{-1}$.

In addition, TOF-SIMS measurement was carried out to evaluate vertical composition distribution in the D18/L8-BO bilayer film based on D18 fabricated under the processing conditions of 60 ℃+TA&SVA. The sample was fabricated on

ITO/PEDOT:PSS substrate. CN^- was the characteristic ionic fragment of L8-BO while SO_3^- and InO^- were those for PEDOT:PSS and ITO from the bottom of the sample, respectively. The TOF-SIMS depth plots and corresponding 3D images were shown in Figure 5 and Figure S6. The bilayer active layer thickness calculated by TOF-SIMS is consistent with that measured by profilometer. The distribution of L8-BO in bilayer film was illustrated through the distribution of the CN^-. The intensity of CN^- anions began to decay slowly when the sputter time was 25 seconds and then became more rapidly at the sputter time of 40 seconds. The intensity of CN^- ionic decayed close to 0 when the SO_3^- anion signal began to rise. The TOF-SIMS depth plots demonstrated that L8-BO penetrated into D18 polymer domain when the L8-BO chloroform solution was spuncast on the top. L8-BO was enriched near the top cathode and D18 mainly existed close to the bottom anode, supporting the formation of vertical phase separation with a D/D:A/A P-i-N structure for efficient charge transport and suppressed charge recombination.

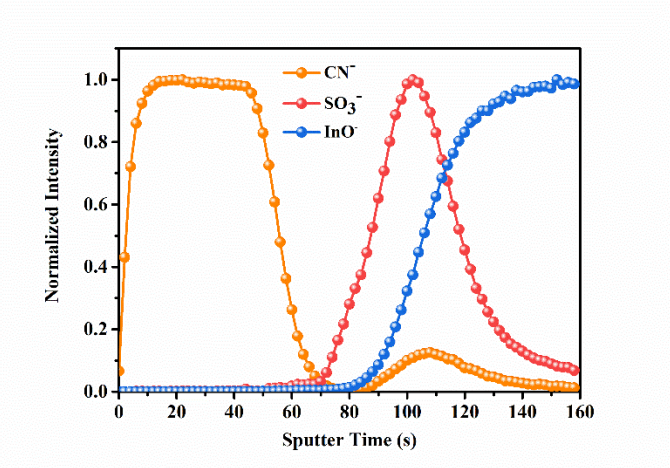

Figure 5. The TOF-SIMS depth plots of D18/L8-BO bilayer film fabricated on PEDOT:PSS/ITO/glass.

Atomic force microscopy (AFM) measurements were also employed to probe the surface morphology of the D18 layer from various processing conditions. As shown in Figure 6 and Figure S7, the D18 film fabricated from the solution at 30 ℃ exhibited large scale aggregation. With the rise of solution temperature, more delicate structures were formed with the root-mean-square (RMS) roughness value decreased from 2.69

to 2.39 nm. After the D18 film (processed from the solution at 60 ℃) was further treated with TA&SVA, the RMS roughness was slightly reduced to 2.26 nm. When the solution temperature reached 90 ℃, the solubility of D18 was significantly increased and the polymer chains became more relaxed, leading to reduced chain aggregation. Therefore, the film fabricated from solution at this temperature showed the smallest RMS roughness of 2.15 nm. In addition, transmission electron microscope (TEM) images of D18 single layer films and D18/L8-BO bilayer films were shown in Figure 6. D18 films processed from solution at 30 ℃ showed larger aggregates due to higher degree of pre-aggregation in solution, while the D18 films under the processing condition of 60 ℃+TA&SVA were more uniform with some fiber-like structures. Under this condition, D18 chain segments maintain good interaction and appropriate chain entanglement, which would be conducive to the penetration of L8-BO acceptors while maintaining good interpenetrating networks. Therefore, D18/L8-BO bilayer fabricated under the condition of 60 ℃+TA&SVA has a more homogeneous structure which is responsible for more efficient exciton dissociation and high photovoltaic performance.

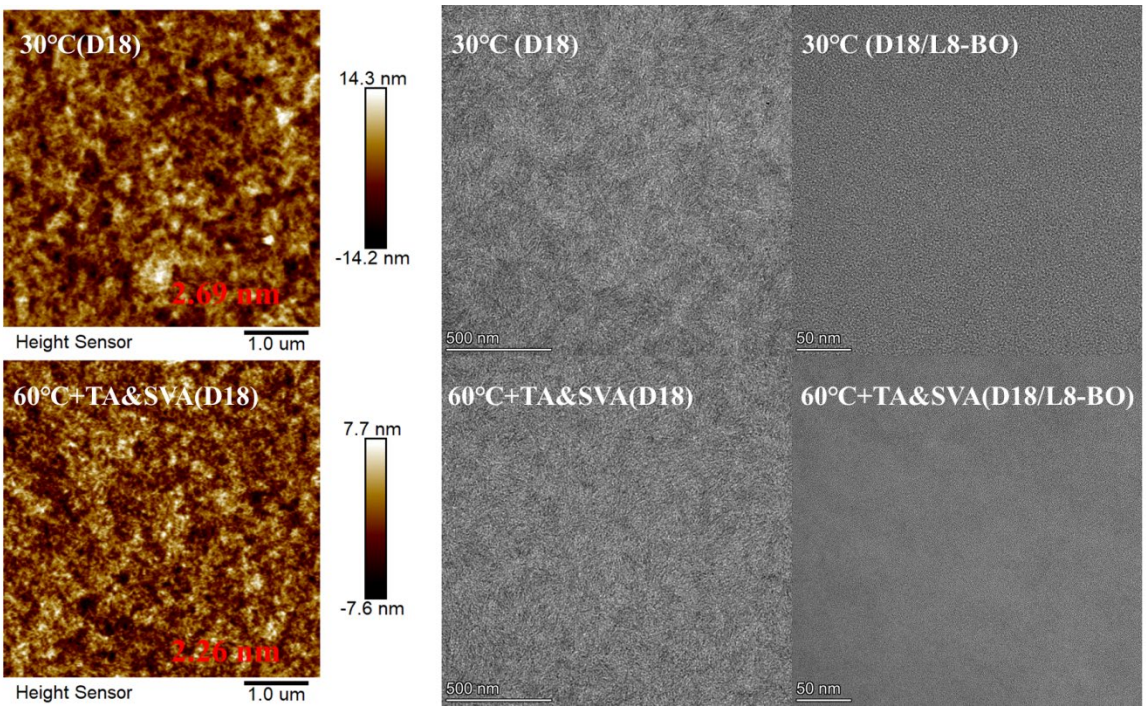

Figure 6. AFM images of D18 single layer films, and TEM images of D18 single layer films and D18/L8-BO bilayer films.

3. Conclusion

In this manuscript, we have demonstrated a facile and effective approach to fabricating D18/L8-BO bilayer films with suitable microstructure and vertical phase separation for highly efficient LBL OSCs. The solution temperature of D18 and the annealing processes of the bilayer film had a remarkable impact on molecular pre-aggregation in solution and microstructures in solid films. D18 bottom layer with a planar stacking and suitable fibril structures in active layer provides a good underlayer for the formation of L8-BO top layer and D-A interface, which are effective for efficient exciton separation and charge transport. PL measurements suggested that the optimized film exhibited suppressed nonradiative recombination and more efficient charge transfer. TA analysis supported that the average size of acceptor phase for the film processed at 60 ℃+TA&SVA was slightly larger than that for the film processed at 30 ℃, and the process condition of 60 ℃+TA&SVA was advantageous for suppressing carrier recombination in the ultrafast timescale. In addition, TOF-SIMS measurement indicated that good vertical phase separation was also realized in the bilayer films. As a result, the optimized LBL OSCs based on D18 and L8-BO delivered an impressively high PCE of 18.02%, which is one of the highest among the reported LBL OSCs and significantly higher than that of the BHJ devices. The features of easy to separately control the morphology of the donor and acceptor layers and to scale up make the LBL method a very promising way to accelerate the commercialization of OSCs.

Conflicts of interest

There are no conflicts to declare.

Acknowledgements

L. X. was supported by the financial support from the National Natural Science Foundation of China (51903057) and we also thank the support from the National Key Research and Development Program of China (2020YFB0408100) and Guangdong Innovative and Entrepreneurial Research Team Program (2016ZT06C412). We would

like to thank Analysis and Test Center of Guangdong University of technology for the UV-vis-NIR and PL spectroscopy measurement. Y.L. acknowledges the support from the Office of Science, Office of Basic Energy Sciences, of the U.S. Department of Energy under Contract No. DE-AC02-05CH11231.

References

(1) Yuan, J.; Zhang, Y.; Zhou, L.; Zhang, G.; Yip, H.-L.; Lau, T.-K.; Lu, X.; Zhu, C.; Peng, H.; Johnson, P. A.; Leclerc, M.; Cao, Y.; Ulanski, J.; Li, Y.; Zou, Y. Single-Junction Organic Solar Cell with over 15% Efficiency Using Fused-Ring Acceptor with Electron-Deficient Core. *Joule* **2019,** *3* (4), 1140-1151.

(2) Li, C.; Zhou, J.; Song, J.; Xu, J.; Zhang, H.; Zhang, X.; Guo, J.; Zhu, L.; Wei, D.; Han, G.; Min, J.; Zhang, Y.; Xie, Z.; Yi, Y.; Yan, H.; Gao, F.; Liu, F.; Sun, Y. Non-fullerene acceptors with branched side chains and improved molecular packing to exceed 18% efficiency in organic solar cells. *Nat. Energy* **2021,** *6* (6), 605-613.

(3) Zhong, W.; Zhang, M.; Zhu, L.; Zhang, Y.; Liu, F. Complex multilength-scale morphology in organic photovoltaics. *Trends Chem* **2022**, DOI:10.1016/j.trechm.2022.05.004.

(4) Xu, T.; Lv, J.; Yang, K.; He, Y.; Yang, Q.; Chen, H.; Chen, Q.; Liao, Z.; Kan, Z.; Duan, T.; Sun, K.; Ouyang, J.; Lu, S. 15.8% efficiency binary all-small-molecule organic solar cells enabled by a selenophene substituted sematic liquid crystalline donor. *Energy Environ. Sci.* **2021,** *14* (10), 5366-5376.

(5) Xiao, L.; Wu, X.; Ren, G.; Kolaczkowski, M. A.; Huang, G.; Tan, W.; Ma, L.; Liu, Y.; Peng, X.; Min, Y.; Liu, Y. Highly Efficient Ternary Solar Cells with Efficient Förster Resonance Energy Transfer for Simultaneously Enhanced Photovoltaic Parameters. *Adv. Funct. Mater.* **2021,** *31* (41), 2105304.

(6) Wu, B.; Yin, B.; Duan, C.; Ding, L. All-polymer solar cells. *Journal of Semiconductors* **2021,** *42* (8), 080301.

(7) Wu, Y.; Guo, J.; Wang, W.; Chen, Z.; Chen, Z.; Sun, R.; Wu, Q.; Wang, T.; Hao, X.; Zhu, H.; Min, J. A conjugated donor-acceptor block copolymer enables over 11% efficiency for single-component polymer solar cells. *Joule* **2021,** *5* (7), 1800-1815.

(8) Zhu, L.; Zhang, M.; Xu, J.; Li, C.; Yan, J.; Zhou, G.; Zhong, W.; Hao, T.; Song, J.; Xue, X.; Zhou, Z.; Zeng, R.; Zhu, H.; Chen, C.-C.; MacKenzie, R. C. I.; Zou, Y.; Nelson, J.; Zhang, Y.; Sun, Y.; Liu, F. Single-junction organic solar cells with over 19% efficiency enabled by a refined double-fibril network morphology. *Nat. Mater.* **2022,** *21* (6), 656-663.

(9) Gao, W.; Qi, F.; Peng, Z.; Lin, F. R.; Jiang, K.; Zhong, C.; Kaminsky, W.; Guan, Z.; Lee, C.-S.; Marks, T. J.; Ade, H.; Jen, A. K. Y. Achieving 19% Power Conversion Efficiency in Planar-Mixed Heterojunction Organic Solar Cells Using a Pseudo-Symmetric Electron Acceptor. *Adv. Mater.* **2022,** DOI:10.1002/adma.202202089.

(10) Zheng, Z.; Wang, J.; Bi, P.; Ren, J.; Wang, Y.; Yang, Y.; Liu, X.; Zhang, S.; Hou, J. Tandem Organic Solar Cell with 20.2% Efficiency. *Joule* **2022,** *6* (1), 171-184.

(11) Yu, G.; Gao, J.; Hummelen, J. C.; Wudl, F.; Heeger, A. J. Polymer Photovoltaic Cells: Enhanced Efficiencies via a Network of Internal Donor-Acceptor Heterojunctions. *Science* **1995,** *270* (5243), 1789-1791.

(12) Hoppe, H.; Sariciftci, N. S. Organic solar cells: An overview. *Journal of Materials Research* **2011,** *19* (7), 1924-1945.

(13) Wan, J.; Zeng, L.; Liao, X.; Chen, Z.; Liu, S.; Zhu, P.; Zhu, H.; Chen, Y. All-Green Solvent-Processed Planar Heterojunction Organic Solar Cells with Outstanding Power Conversion Efficiency of 16%. *Adv. Funct. Mater.* **2022,** *32* (5), 2107567.

(14) Zhang, G.; Zhao, J.; Chow, P. C. Y.; Jiang, K.; Zhang, J.; Zhu, Z.; Zhang, J.; Huang, F.; Yan, H. Nonfullerene Acceptor Molecules for Bulk Heterojunction Organic Solar Cells. *Chem. Rev.* **2018,** *118* (7), 3447-3507.

(15) Yan, C.; Barlow, S.; Wang, Z.; Yan, H.; Jen, A. K. Y.; Marder, S. R.; Zhan, X. Non-fullerene acceptors for organic solar cells. *Nat. Rev. Mater.* **2018,** *3* (3), 18003, DOI: 10.1038/natrevmats.2018.3.

(16) Hou, J.; Inganäs, O.; Friend, R. H.; Gao, F. Organic solar cells based on non-fullerene acceptors. *Nat. Mater.* **2018,** *17* (2), 119-128.

(17) Cheng, P.; Li, G.; Zhan, X.; Yang, Y. Next-generation organic photovoltaics based on non-fullerene acceptors. *Nat. Photonics* **2018,** *12* (3), 131-1429.

(18) Cui, C.; Li, Y. Morphology optimization of photoactive layers in organic solar cells. *Aggregate* **2021,** *2* (2), e31.

(19) Chen, H.; Zhao, T.; Li, L.; Tan, P.; Lai, H.; Zhu, Y.; Lai, X.; Han, L.; Zheng, N.; Guo, L.; He, F. 17.6%-Efficient Quasiplanar Heterojunction Organic Solar Cells from a Chlorinated 3D Network Acceptor. *Adv. Mater.* **2021,** *33* (37), 2102778.

(20) Wei, Y.; Chen, Z.; Lu, G.; Yu, N.; Li, C.; Gao, J.; Gu, X.; Hao, X.; Lu, G.; Tang, Z.; Zhang, J.; Wei, Z.; Zhang, X.; Huang, H. Binary Organic Solar Cells Breaking 19% via Manipulating Vertical

Component Distribution. *Adv. Mater.* **2022,** DOI:10.1002/adma.202204718.

(21) Fu, H.; Gao, W.; Li, Y.; Lin, F.; Wu, X.; Son, J. H.; Luo, J.; Woo, H. Y.; Zhu, Z.; Jen, A. K. Y. A Generally Applicable Approach Using Sequential Deposition to Enable Highly Efficient Organic Solar Cells. *Small Methods* **2020,** *4* (12), 2000687.

(22) Dong, S.; Zhang, K.; Xie, B.; Xiao, J.; Yip, H.-L.; Yan, H.; Huang, F.; Cao, Y. High-Performance Large-Area Organic Solar Cells Enabled by Sequential Bilayer Processing via Nonhalogenated Solvents. *Adv. Energy Mater.* **2019,** *9* (1), 1802832.

(23) Sun, R.; Wu, Q.; Guo, J.; Wang, T.; Wu, Y.; Qiu, B.; Luo, Z.; Yang, W.; Hu, Z.; Guo, J.; Shi, M.; Yang, C.; Huang, F.; Li, Y.; Min, J. A Layer-by-Layer Architecture for Printable Organic Solar Cells Overcoming the Scaling Lag of Module Efficiency. *Joule* **2020,** *4* (2), 407-419.

(24) Li, M.; Wang, Q.; Liu, J.; Geng, Y.; Ye, L. Sequential deposition enables high-performance nonfullerene organic solar cells. *Mater. Chem. Front.* **2021,** *5* (13), 4851-4873.

(25) Yu, R.; Wei, X.; Wu, G.; Tan, Z. a. Layer-by-layered organic solar cells: Morphology optimizing strategies and processing techniques. *Aggregate* **2022,** *3* (3), e107.

(26) Li, B.; Zhang, X.; Wu, Z.; Yang, J.; Liu, B.; Liao, Q.; Wang, J.; Feng, K.; Chen, R.; Woo, H. Y.; Ye, F.; Niu, L.; Guo, X.; Sun, H. Over 16% efficiency all-polymer solar cells by sequential deposition. *Sci. Chi. Chem.* **2022,** *65* (6), 1157-1163.

(27) Li, X.; Cao, L.; Yu, X.; Du, X.; Lin, H.; Yang, G.; Chen, Z.; Zheng, C.; Tao, S. High-Efficiency Sequential-Cast Organic Solar Cells Enabled by Dual Solvent-Controlled Polymer Aggregation. *Sol. RRL* **2022,** *6* (6), 2200076.

(28) Li, Q.; Jia, T.; Wang, L.-M.; Liu, S.; Liao, X.; Cao, Z.; Zhang, J.; Zhan, X.; Zhu, T.; Cai, Y.-P.; Huang, F. Superior layer-by-layer deposition realizing P–i–N all-polymer solar cells with efficiency over 16% and fill factor over 77%. *J. Mater. Chem. A.* **2022,** *10* (20), 10880-10891.

(29) Zhang, Y.; Wu, B.; He, Y.; Deng, W.; Li, J.; Li, J.; Qiao, N.; Xing, Y.; Yuan, X.; Li, N.; Brabec, C. J.; Wu, H.; Lu, G.; Duan, C.; Huang, F.; Cao, Y. Layer-by-layer processed binary all-polymer solar cells with efficiency over 16% enabled by finely optimized morphology. *Nano Energy* **2022,** *93*, 106858.

(30) Xu, Y.; Yuan, J.; Liang, S.; Chen, J.-D.; Xia, Y.; Larson, B. W.; Wang, Y.; Su, G. M.; Zhang, Y.; Cui, C.; Wang, M.; Zhao, H.; Ma, W. Simultaneously Improved Efficiency and Stability in All-Polymer Solar Cells by a P–i–N Architecture. *Acs. Energy Lett.* **2019,** *4* (9), 2277-2286.

(31) Zhan, L.; Li, S.; Xia, X.; Li, Y.; Lu, X.; Zuo, L.; Shi, M.; Chen, H. Layer-by-Layer Processed Ternary

Organic Photovoltaics with Efficiency over 18%. *Adv. Mater.* **2021,** *33* (12), 2007231.

(32) Xu, W.; Ma, X.; Son, J. H.; Jeong, S. Y.; Niu, L.; Xu, C.; Zhang, S.; Zhou, Z.; Gao, J.; Woo, H. Y.; Zhang, J.; Wang, J.; Zhang, F. Smart Ternary Strategy in Promoting the Performance of Polymer Solar Cells Based on Bulk-Heterojunction or Layer-By-Layer Structure. *Small* **2022,** *18* (4), 2104215.

(33) Wang, X.; Zhang, L.; Hu, L.; Xie, Z.; Mao, H.; Tan, L.; Zhang, Y.; Chen, Y. High-Efficiency (16.93%) Pseudo-Planar Heterojunction Organic Solar Cells Enabled by Binary Additives Strategy. *Adv. Funct. Mater.* **2021,** *31* (33), 2102291.

(34) Xu, X.; Yu, L.; Meng, H.; Dai, L.; Yan, H.; Li, R.; Peng, Q. Polymer Solar Cells with 18.74% Efficiency: From Bulk Heterojunction to Interdigitated Bulk Heterojunction. *Adv. Funct. Mater.* **2022,** *32* (4), 2108797.

(35) Karuthedath, S.; Firdaus, Y.; Scaccabarozzi, A. D.; Nugraha, M. I.; Alam, S.; Anthopoulos, T. D.; Laquai, F. Trace Solvent Additives Enhance Charge Generation in Layer-by-Layer Coated Organic Solar Cells. *Small Structures* **2022,** *3* (4), 2100199.

(36) Yu, R.; Wu, G.; Cui, Y.; Wei, X.; Hong, L.; Zhang, T.; Zou, C.; Hu, S.; Hou, J.; Tan, Z. a. Multi-Functional Solid Additive Induced Favorable Vertical Phase Separation and Ordered Molecular Packing for Highly Efficient Layer-by-Layer Organic Solar Cells. *Small* **2021,** *17* (44), 2103497.

(37) Ning, H.; Jiang, Q.; Han, P.; Lin, M.; Zhang, G.; Chen, J.; Chen, H.; Zeng, S.; Gao, J.; Liu, J. Manipulating the solubility properties of polymer donors for high-performance layer-by-layer processed organic solar cells. *Energy Environ. Sci.* **2021,** *14* (11), 5919-5928.

(38) Wei, Y.; Yu, J.; Qin, L.; Chen, H.; Wu, X.; Wei, Z.; Zhang, X.; Xiao, Z.; Ding, L.; Gao, F. A universal method for constructing high efficiency organic solar cells with stacked structures. *Energy Environ. Sci.* **2021,** *14* (4), 2314-2321.

(39) Yao, Z.-F.; Wang, J.-Y.; Pei, J. High-performance polymer field-effect transistors: from the perspective of multi-level microstructures. *Chem. Sci.* **2021,** *12* (4), 1193-1205.

(40) Zhao, H.; Naveed, H. B.; Lin, B.; Zhou, X.; Yuan, J.; Zhou, K.; Wu, H.; Guo, R.; Scheel, M. A.; Chumakov, A.; Roth, S. V.; Tang, Z.; Müller-Buschbaum, P.; Ma, W. Hot Hydrocarbon-Solvent Slot-Die Coating Enables High-Efficiency Organic Solar Cells with Temperature-Dependent Aggregation Behavior. *Adv. Mater.* **2020,** *32* (39), 2002302.

(41) Zhu, L.; Zhong, W.; Qiu, C.; Lyu, B.; Zhou, Z.; Zhang, M.; Song, J.; Xu, J.; Wang, J.; Ali, J.; Feng, W.; Shi, Z.; Gu, X.; Ying, L.; Zhang, Y.; Liu, F. Aggregation-Induced Multilength Scaled Morphology

Enabling 11.76% Efficiency in All-Polymer Solar Cells Using Printing Fabrication. *Adv. Mater.* **2019,** *31* (41), 1902899.

(42) Yang, C.; Liang, N.; Ye, L.; Ade, H.; Yuan, X.; Hou, J. Enhanced JSC of P3HT-based non-fullerene polymer solar cells by modulating aggregation effect of P3HT in solution state. *Org. Electron.* **2019,** *68*, 15-21.

(43) Li, M.; Balawi, A. H.; Leenaers, P. J.; Ning, L.; Heintges, G. H. L.; Marszalek, T.; Pisula, W.; Wienk, M. M.; Meskers, S. C. J.; Yi, Y.; Laquai, F.; Janssen, R. A. J. Impact of polymorphism on the optoelectronic properties of a low-bandgap semiconducting polymer. *Nat. Commun.* **2019,** *10* (1), 2867.

(44) Guo, C.; Li, D.; Wang, L.; Du, B.; Liu, Z.-X.; Shen, Z.; Wang, P.; Zhang, X.; Cai, J.; Cheng, S.; Yu, C.; Wang, H.; Liu, D.; Li, C.-Z.; Wang, T. Cold-Aging and Solvent Vapor Mediated Aggregation Control toward 18% Efficiency Binary Organic Solar Cells. *Adv. Energy Mater.* **2021,** *11* (39), 2102000.

(45) Kim, Y.-J.; Kim, N.-K.; Park, W.-T.; Liu, C.; Noh, Y.-Y.; Kim, D.-Y. Kinetically Controlled Crystallization in Conjugated Polymer Films for High-Performance Organic Field-Effect Transistors. *Adv. Funct. Mater.* **2019,** *29* (23), 1807786.

(46) Zhao, J.; Li, Y.; Yang, G.; Jiang, K.; Lin, H.; Ade, H.; Ma, W.; Yan, H. Efficient organic solar cells processed from hydrocarbon solvents. *Nat. Energy* **2016,** *1* (2), 15027, DOI: 10.1038/nenergy.2015.27.

(47) Jin, K.; Xiao, Z.; Ding, L. D18, an eximious solar polymer! *Journal of Semiconductors* **2021,** *42* (1), 010502.

(48) Song, J.; Zhu, L.; Li, C.; Xu, J.; Wu, H.; Zhang, X.; Zhang, Y.; Tang, Z.; Liu, F.; Sun, Y. High-efficiency organic solar cells with low voltage loss induced by solvent additive strategy. *Matter* **2021,** *4* (7), 2542-2552.

(49) Cao, X.; Zhao, K.; Chen, L.; Liu, J.; Han, Y. Conjugated polymer single crystals and nanowires. *POLYMER CRYSTALLIZATION* **2019,** *2* (3), e10064.

(50) Zheng, Y.; Sun, R.; Zhang, M.; Chen, Z.; Peng, Z.; Wu, Q.; Yuan, X.; Yu, Y.; Wang, T.; Wu, Y.; Hao, X.; Lu, G.; Ade, H.; Min, J. Baseplate Temperature-Dependent Vertical Composition Gradient in Pseudo-Bilayer Films for Printing Non-Fullerene Organic Solar Cells. *Adv. Energy Mater.* **2021,** *11* (45), 2102135.

(51) Ma, Y.; Cai, D.; Wan, S.; Wang, P.; Wang, J.; Zheng, Q. Ladder-Type Heteroheptacenes with Different Heterocycles for Nonfullerene Acceptors. *Angew. Chem. Int. Edit.* **2020,** *132* (48), 21811-21817.

(52) Li, Z.; Yan, C.; Xiao, L.; Mao, H.; Liu, J.; Tan, W.; Min, Y. Small molecule ternary solar cell with

two synergistic electron acceptors for enhanced photovoltaic performance. *Org. Electron.* **2021,** *93*, 106135.

(53) Mihailetchi, V. D.; Xie, H. X.; de Boer, B.; Koster, L. J. A.; Blom, P. W. M. Charge Transport and Photocurrent Generation in Poly(3-hexylthiophene): Methanofullerene Bulk-Heterojunction Solar Cells. *Adv. Funct. Mater.* **2006,** *16* (5), 699-708.

(54) Cowan, S. R.; Roy, A.; Heeger, A. J. Recombination in polymer-fullerene bulk heterojunction solar cells. *Phys Rev B* **2010,** *82* (24), 245207.

(55) Koster, L. J. A.; Mihailetchi, V. D.; Ramaker, R.; Blom, P. W. M. Light intensity dependence of open-circuit voltage of polymer:fullerene solar cells. *Appl. Phys. Lett.* **2005,** *86* (12), 123509.

(56) Li, D.; Zhu, L.; Liu, X.; Xiao, W.; Yang, J.; Ma, R.; Ding, L.; Liu, F.; Duan, C.; Fahlman, M.; Bao, Q. Enhanced and Balanced Charge Transport Boosting Ternary Solar Cells Over 17% Efficiency. *Adv. Mater.* **2020,** *32* (34), 2002344.

(57) Jiang, K.; Zhang, J.; Peng, Z.; Lin, F.; Wu, S.; Li, Z.; Chen, Y.; Yan, H.; Ade, H.; Zhu, Z.; Jen, A. K. Y. Pseudo-bilayer architecture enables high-performance organic solar cells with enhanced exciton diffusion length. *Nat. Commun.* **2021,** *12* (1), 468.

(58) Song, J.; Li, C.; Zhu, L.; Guo, J.; Xu, J.; Zhang, X.; Weng, K.; Zhang, K.; Min, J.; Hao, X.; Zhang, Y.; Liu, F.; Sun, Y. Ternary Organic Solar Cells with Efficiency >16.5% Based on Two Compatible Nonfullerene Acceptors. *Adv. Mater.* **2019,** *31* (52), 1905645.

(59) Xiao, L. G.; He, B.; Hu, Q.; Maserati, L.; Zhao, Y.; Yang, B.; Kolaczkowski, M. A.; Anderson, C. L.; Borys, N. J.; Klivansky, L. M.; Chen, T. L.; Schwartzberg, A. M.; Russell, T. P.; Cao, Y.; Peng, X. B.; Liu, Y. Multiple Roles of a Non-fullerene Acceptor Contribute Synergistically for High-Efficiency Ternary Organic Photovoltaics. *Joule* **2018,** *2* (10), 2154-2166.

(60) Zhou, G.; Zhang, M.; Xu, J.; Yang, Y.; Hao, T.; Zhu, L.; Zhou, L.; Zhu, H.; Zou, Y.; Wei, G.; Zhang, Y.; Liu, F. Spontaneous carrier generation and low recombination in high-efficiency non-fullerene solar cells. *Energy Environ. Sci.* **2022,** *15* (8), 3483-3493.

(61) Wu, Q.; Wang, W.; Wu, Y.; Chen, Z.; Guo, J.; Sun, R.; Guo, J.; Yang, Y.; Min, J. High-Performance All-Polymer Solar Cells with a Pseudo-Bilayer Configuration Enabled by a Stepwise Optimization Strategy. *Adv. Funct. Mater.* **2021,** *31* (15), 2010411.

Table of Content